Ultrasonic crack evaluation by phase coherence processing and TFM and its application to online monitoring in fatigue tests

J. Camacho[1*], D. Atehortua[2], J. F. Cruza[1], J. Brizuela[3], J. Ealo[2].

[1] Spanish National Research Council, Madrid, Spain

J. Camacho: j.camacho@csic.es (corresponding author);

J. F. Cruza: jorge.f.cruza@csic.es

[2] Universidad del Valle, Cali, Colombia

D. Atehortua:daniel.atehortua@correounivalle.edu.co;

J. Ealo: joao.ealo@correounivalle.edu.co

[3] National Scientific and Technical Research Council, Buenos Aires, Argentina

J. Brizuela :josebrizuela@conicet.gov.ar

* Author to whom correspondence should be addressed; E-Mail: j.camacho@csic.es

Abstract

This work proposes a new ultrasonic imaging method for crack evaluation with arrays, and investigates its application to online monitoring of crack propagation in fatigue tests. The Total Focusing Method (TFM) is used to obtain the best possible image of the crack propagation path and orientation, while Phase Coherence Imaging (PCI) is used to precisely determining its length by accurately locating the tips position. Experimental verification was performed with a 15 MHz array and a set of 4 samples tested up to different crack lengths by cyclic loading. Crack orientation and length obtained with the proposed method showed good matching with optical measurements, and sizing by tip detection with PCI was more robust than amplitude-drop sizing with TFM.

Keywords

ultrasound; crack sizing; total focusing method; phase coherence imaging; fatigue test.

1. INTRODUCTION

Crack detection and sizing is an important topic for non-destructive testing field (NDT). Quality control of some production processes, like welding, require detecting the presence of cracks generated during the manufacturing process. For in-service components, detection and monitoring of cracks propagation gives valuable information for maintenance programs and can be used to predict the remaining life of components. In this context, crack propagation tests are usually carried out in order to characterize material resistance of samples to stable crack extension under cyclic loading conditions.

Ultrasonic techniques are among the most extended for defects detection and characterization. By propagating high frequency mechanical waves into the material and analyzing the received echoes, information about the component condition and possible defects is obtained. This work proposes a new ultrasonic imaging method for crack evaluation with arrays, and investigates its application to online monitoring of crack propagation in fatigue tests.

1.1. Ultrasonic methods for crack length estimation

One of the most extended techniques for accurate crack sizing with ultrasound is Time-Of-Flight Diffraction (TOFD). Here, a pair of small size transducers is used in a pitch-catch configuration to insonify the whole volume of the sample under test and to register the waves diffracted by the crack tips [1-2]. This way, the measured size does not depend on the crack reflectivity, coupling condition or transducer sensitivity, as it happens in amplitude-drop based methods [3-5]. By laterally moving both transducers along the inspected component a B-Scan image is generated, where each tip follows a trajectory given by the time-of-flight dependency with the lateral position of the transducers. This fact has been exploited to improve the measurement resolution in the movement direction by Synthetic Aperture Focusing (SAFT), combining several consecutive A-Scans to obtain each B-Scan pixel after applying a set of focusing delays [6]. For a given emitter-to-receiver time-of-flight, the geometric locus of the reflector in the transducers plane is an ellipse with foci at the transducers position, and hence, the real location of the reflector cannot be univocally determined [7]. Usually, TOFD standards assume that all the tips are located in the transverse plane half-way between both transducers (vertical crack propagation) to give readings of crack equivalent length and depth. In the case of online monitoring in fatigue tests, this approach is not valid, because the crack length and its orientation must be accurately determined. Furthermore, considering the relatively small size of fatigue test samples, it is not always possible to find a suitable TOFD pitch-catch configuration.

Phased-array (PA) imaging has been used to image diffraction tips with high sensitivity and resolution [8-10]. By emitting a focused beam, the diffraction tip can be observed even in materials with high grain-noise level, where conventional transducers or TOFD find difficult to distinguish the tip from the background scattering. Furthermore, PA has the advantage of operating in pulse-echo, which simplifies the mechanical setup, especially in reduced size samples. The main limitation of PA for crack evaluation is that, excluding the tip, most of the crack behaves like a specular reflector, producing a significant echo only when the beam direction is perpendicular to the crack path. The consequence is that usually the crack propagation path cannot be followed in all its extension with a single sector image (S-Scan).

The Total Focusing Method (TFM) overcomes the beam-directivity limitation of PA by emitting with a single element and receiving individually with all of them [11-12]. Then a low-resolution image is constructed by delay-and-sum (DAS) beamforming, and the process is repeated emitting with a different element. After all the array elements are used as emitters, the set of low-resolution images is averaged to get a high-resolution image dynamically focused in emission and in reception, which could be considered the gold-standard for DAS beamformers. The set of all acquired signals during the process is named Full Matrix Capture (FMC).

Regarding PA, TFM has the advantage of not having a preferential propagation direction. On the contrary, combining omnidirectional emissions with all the array elements ensures that a planar defect will be detected regardless its orientation, provided that its inclination angle and vertical distance to the array are compatible to receive some specular reflection. Furthermore, dynamic focusing in emission and reception avoid the complication of precisely locating the PA emission focus to follow the crack growth or, alternatively, sacrificing lateral resolution by reducing the emission aperture to increase the depth of field.

While TFM can provide precise information of the crack propagation path and orientation [13], crack size estimation based on conventional amplitude drop methods may be not accurate. In [14], an alternative model-based crack sizing algorithm is given, which relies on the Born approximation and an optimization process to obtain the crack length and orientation. In [15-16] the scattering matrix concept is used as a tool for defect characterization. Scattering coefficient matrices describe the signal scattered by a defect as a function of incident and scattered angles, giving information about defect geometry, orientation and size.

On the other hand, Phase Coherence Imaging (PCI) was proposed to improve the resolution and contrast of ultrasound images [17-18]. PCI performs an adaptive beamforming by weighting the aperture data by a coherence factor (PCF) obtained from the instantaneous phase dispersion along the array elements. If all signals come from an ideal point-like reflector at the focus, their instantaneous phases will be equal, coherence factor will be unity and the echo signal will be kept in the output image. On the other hand, if the reflector is not at focus, the phase dispersion along the aperture increases and the coherence factor reduces the indication amplitude in the output image.

As it was pointed out in [19] and it is further addressed in this work, PCF values are also less than unity for non-point-like reflectors, regardless if they are located or not at the focus. In the case of a crack, its central region will be attenuated by PCI, but the diffraction tips, which behave as point-like reflectors, will be kept. This fact is exploited here for the first time, proposing a phase coherence based method to perform crack length measurements from the FMC dataset. Furthermore, the coherence factor is used to construct a new image instead of using it to weight the reflectivity image. While the TFM image gives information about the crack path, the coherence image precisely locates the crack tip. Both images are obtained from the same dataset.

1.2. Online monitoring in fatigue tests

Fatigue crack propagation tests are carried out to characterize material resistance of samples to stable crack extension under cyclic loading conditions [20]. This way, crack propagation rates can be computed and the design of strategies for increasing component longevity is possible, which has been the target of plentiful studies concerning applications where crack propagation stage takes most of the service life of components. This is particularly true for some weld joints such as seams and girth weld toes, cover plate fillet weld terminations and stiffeners found in bridges, pressure vessels, ships and offshore structures [21]. However, performing fatigue crack propagation tests in weld joints, for instance, is problematic and results might be easily misunderstood due to influence of several factors and limitations that are normally present because of the welding process itself [22]. In view of this, the ASTM E647-

13ae1 test standard allows to employ Compact Tension (CT) samples to propagate cracks in a controlled and repetitive way. Recently, physical simulation of samples is being used as a tool in an effort to isolate the main factors affecting crack propagation behavior. For instance, in Figure 1, the geometry of a CT sample, in accordance to the standard, is used in the study of the effect of the microstructure on crack propagation rates in steel weld joints [23]. Cyclic loading is applied, perpendicular to the expected crack path, by means of the two 9.9 mm diameter through-holes shown.

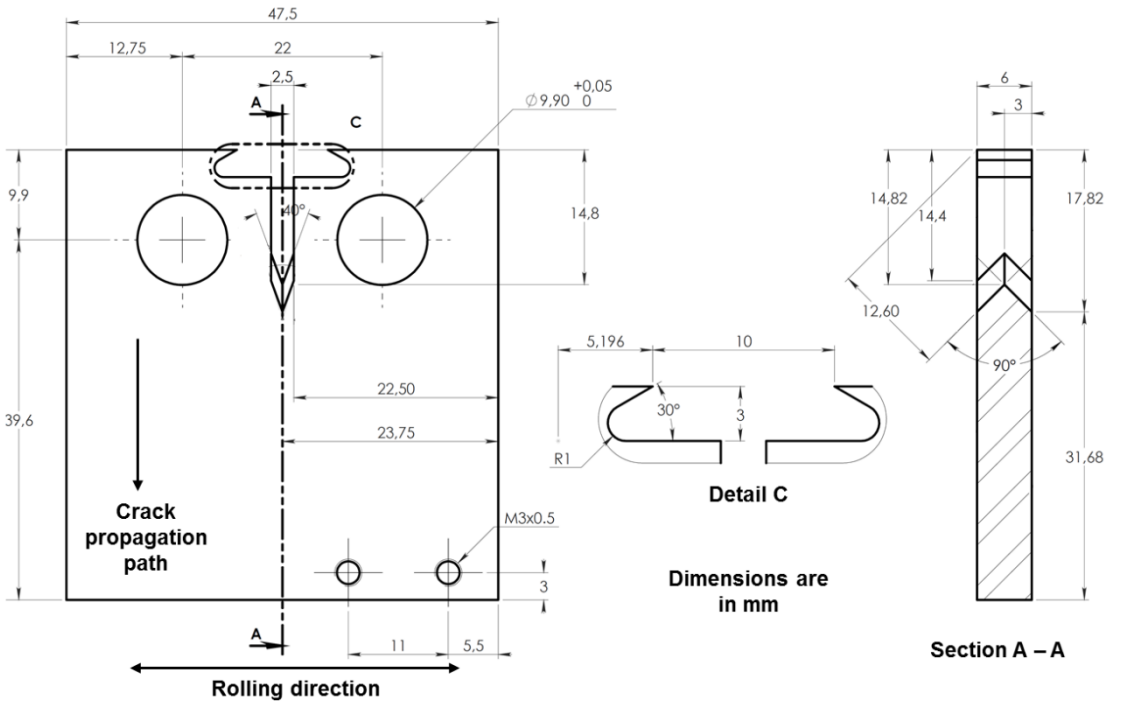

Figure 1. Detailed drawing of a CT sample used for fatigue crack propagation testing of steel weld joints under ASTM E647 – 13ae1test standard.

According to ASTM test standard, crack length monitoring methods explicitly include direct (visual) and indirect measurements (compliance and electric potential difference). The implementation of any of these methods is not an easy task. Crack length measurement might be even more difficult to perform because a calibration procedure is required at the beginning of the test and for every sample. At the end of the test, verification must be carried out by means of a post mortem macroscopic examination of the propagated crack surface features. Very often, corrections due to crack tunneling or other crack behaviors are required to obtain coherent final results. As a matter of fact, the standard methods included in the ASTM E647 are not fully reliable, and impractical to some extent, for online crack length determination. Furthermore, crack deviation angle, if present, can only be detected by periodic visual inspection of crack path during test, which is prone to errors. Besides, crack closure effect is not easy to be noticed and consequently it is hard to be determined from experimental measurements.

Compliance method is sensitive to size and material of the sample. Crack length determination through this method is usually carried out by means of a clip-on gage properly placed on crack mouth. Laser interferometry [24] can also be used to measure crack opening displacement. However, it is more expensive, less common and is mainly addressed to small crack monitoring, which is not the scope of this work. Visual

inspection is also sensitive to size and is used for small thickness samples. Potential difference method is good for small size probes, but for thick samples, e.g. 1 inch, a more complex setup is required and heating could be an issue. Consequently, crack length estimation is not feasible when industrial scale extrapolation of standard methods is intended.

On the other hand, nonstandard methods based on nondestructive testing techniques have been developed to monitor crack length during fatigue tests. Among them, surface acoustic wave [25-27] and acoustic emission [28-30] have been fairly used for that purpose. However, no information is provided about crack orientation and some of the implementations are only suitable for small crack growth behavior. Recently, crack imaging has emerged as an innovative tool. Magnetic flux leakage and eddy current pulsed thermography [31] and X-Ray computed tomography [32] have been proposed. Although different works have also been reported using ultrasound [33-34], this work proposes to use a new ultrasonic method based on PCI that could be used as an online monitoring tool for crack propagation path measurement during fatigue crack propagation tests.

An approximated mathematical formulation for the simplest case of a large horizontal crack is given, with the objective of better understanding the PCI working principle for detecting the crack tip. Then, more complex scenarios including different crack sizes and orientations are analyzed by numerical simulation. Finally, experimental results with a set of 4 samples subjected to standard fatigue tests are presented and compared with results obtained from visual inspection method.

2. THE IMAGING METHOD

Figure 2 schematically depicts the image formation process in TFM. When emitting with element i and receiving with element k, the time-of-flight t_{ikP} to an arbitrary image pixel P at coordinates (x,z) is

$$t_{ikP} = \frac{\left|\vec{r}_{iP}\right| + \left|\vec{r}_{kP}\right|}{c} \tag{1}$$

where $\vec{r}_{iP}$ and $\vec{r}_{kP}$ are the distances from the pixel to the emitter and the receiver elements respectively, and c is the speed of sound in the material. The TFM image value at pixel P is obtained by

$$I_P = \frac{1}{N^2}\left|\sum_{i=1}^{N}\sum_{k=1}^{N} S_{ik}\left(t_{ikP}\right)\right| \tag{2}$$

where N is the number of elements of the array, $S_{ik}(t)$ is the analytic representation of the signal received by element k when emitting with element i(i,k position of the FMC matrix), obtained from the real valued received signal $s_{ik}(t)$ by application of the Hilbert Transform $H(\cdot)$:

$$S_{ik}\left(t\right) = s_{ik}\left(t\right) + j \cdot H\left(s_{ik}\left(t\right)\right) \tag{3}$$

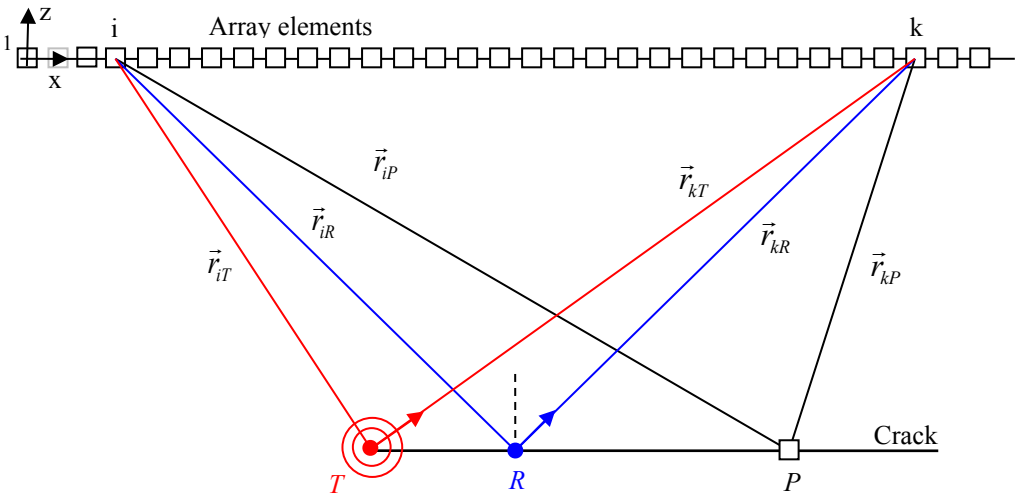

Figure 2 – Schematic representation of the TFM beamforming geometry for imaging a horizontal crack, where *T*, *R* and *P* are the locations of the tip, the specular reflection and the imaged pixel respectively.

The Sign Coherence Factor (SCF) was defined in [17] as an alternative to the coherence factor based on the instantaneous phase of the received signals (PCF). With similar results than PCF and a simpler implementation (based on the sign of the received signals), SCF is the preferred realization for NDT applications. After emitting with element *i*, the SCF for pixel *P* is given by:

$$SCF_{iP} = 1 - \sqrt{1 - \left[\frac{1}{N}\sum_{k=1}^{N} b_{ikP}\right]^2} \tag{4}$$

where b_{ikP} is the sign of the signal received by element *k* at time t_{ikP},

$$b_{ikP} = \begin{matrix} +1 & if & s_{ik}(t_{ikP}) \geq 0 \\ -1 & if & s_{ik}(t_{ikP}) < 0 \end{matrix} \tag{5}$$

In [17] each partial TFM image was weighted by its own coherence factor SCF_i given by (4), before averaging them to obtain the processed TFM image

$$I_P^{SCF} = \frac{1}{N^2}\left|\sum_{i=1}^{N}\left(SCF_{iP}\cdot\sum_{k=1}^{N} S_{ik}(t_{ikP})\right)\right| \tag{6}$$

suppressing side-lobes and improving lateral resolution. In this work, the coherence factors are not used to weight the TFM image. Instead, an independent Sign Coherence Image (SCI) is computed by averaging the coherence factors at every pixel P:

$$SCI_P = \frac{1}{N}\sum_{i=1}^{N} SCF_{iP} \tag{7}$$

The purpose of defining the new term SCI is to emphasize that treating the average coherence factor as an image itself is different from weighting the TFM partial images

by their coherence factors (eq. (6)). As the TFM image is not used in (7), the SCI value will be more related to the reflector coherence than to its echo amplitude, which would enhance weak reflectors like the crack tips.

For an ideal point-like reflector located at P, the focusing delays t_{ikP} compensate the round-trip time-of-flight for all the array elements, all the signs are equal and SCI = 1. But in the case of a plane defect (crack), the strongest echo usually comes from the specular reflection point R, between emitter and receiver elements, which is unlikely to coincide with the pixel position (see Figure 2). This way, when $R \neq P$ the focusing delays do not compensate the round-trip time-of-flight, the received signals become misaligned and SCI < 1.

The question is whether SCI will show the crack tip. On one hand a tip behaves as a point-like reflector and SCI should preserve it. On the other, it is located next to a crack that reflects higher amplitude specular signals with similar time of flight. The interference of these higher level specular signals can distort the received phase distribution of the tip echo, reducing its coherence value.

Although real cracks are not perfectly specular reflectors and their scattering behavior is usually complex, the analysis of the simplest case depicted in Figure 2 (only valid for large horizontal smooth cracks) is useful to understand the working principle of the proposed method. For a signal emitted by element i

$$e_i(t) = E(t)\cos(\omega t) \tag{8}$$

with $E(t)$ the envelope (assumed Gaussian and with unit amplitude), $\omega = 2\pi f$ with f the array center frequency, the signal received by element k from points T (tip) and R (the midway reflecting point) can be modeled by

$$s_{ik}(t) = A_R E(t - t_{ikR})\cos(\omega(t - t_{ikR})) + A_T E(t - t_{ikT})\cos(\omega(t - t_{ikT})) + \eta_{ik}(t) \tag{9}$$

where A_R and A_T are the amplitudes of the crack and tip echoes respectively (usually $A_T << A_R$), t_{ikP} and t_{ikT} the round-tip times of flight to T and R respectively (see figure 2) and $\eta_{ik}(t)$ an uncorrelated noise signal with standard normal distribution and variance σ_η^2. This is a coarse simplification of the impulse response of a horizontal crack, which assumes that only two singular points generate relevant signals in the receiving element: The mid-point between emitter and receiver (specular reflection), and the tip of the crack (omnidirectional diffraction). In this sense, the terms A_R and A_T are positive valued scalars that represent the amplitudes of the reflected waves, and they are not the reflectivity function of the crack (which would be frequency and angle dependent).

After applying the focusing delays t_{ikP} for pixel P, the signal samples used to calculate the *SCI* are

$$s_{ikP} = A_R E(t_{ikP} - t_{ikR})\cos(\omega(t_{ikP} - t_{ikR})) + A_T E(t_{ikP} - t_{ikT})\cos(\omega(t_{ikP} - t_{ikT})) + \eta_{ik}(t_{ikP}) \tag{10}$$

When imaging the crack tip ($P = T$), the focusing delays exactly compensate the time of flight from all array elements to T ($t_{ikP} = t_{ikT}$), and (10) simplifies to

$$s_{ikT} = A_R E(t_{ikT} - t_{ikR})\cos(\omega(t_{ikT} - t_{ikR})) + A_T + \eta_{ik}(t_{ikT}) \tag{11}$$

This leads to an interesting interpretation. When focusing at the tip, an offset A_T appears in the aperture data, which results in more elements giving a positive valued signal. This has the effect of increasing the sign coherence value in the tip with regard to that in the crack, depending on the tip-to-crack reflectivity ratio.

A simulation was performed with a similar configuration to that of the experimental work, i.e. an array of $N = 128$ elements, central frequency $f = 15$ *MHz*, pitch $d = 0.25$ *mm*, relative bandwidth b_w=*60%* (Gaussian envelope) and speed of sound in the tested part $c = 5.9$ *mm/*μs. The emitted signal is assumed to have unit amplitude, and the origin of coordinates is located at element 1 (see Figure 2). A horizontal infinite length crack (no tips) is assumed at z = -25 mm, with specular reflectivity $A_R = 1$. The simulated noise standard deviation is $\sigma_\eta = -40$ *dB*. The specular reflection point is located at $R = (x_{ik}$, -25 mm), with x_{ik} the midpoint between the emitter i and the receiver k.

Figure 3.a shows the samples amplitude s_{ikP} at each array element k (aperture data) when emitting with element $i = 1$ and focusing at pixel $P = (0, -25\ mm)$. In other words, it represents the contribution of each array element to the TFM partial image at pixel P, and was obtained by (10) with $A_T = 0$ (infinite length reflector with no tip).

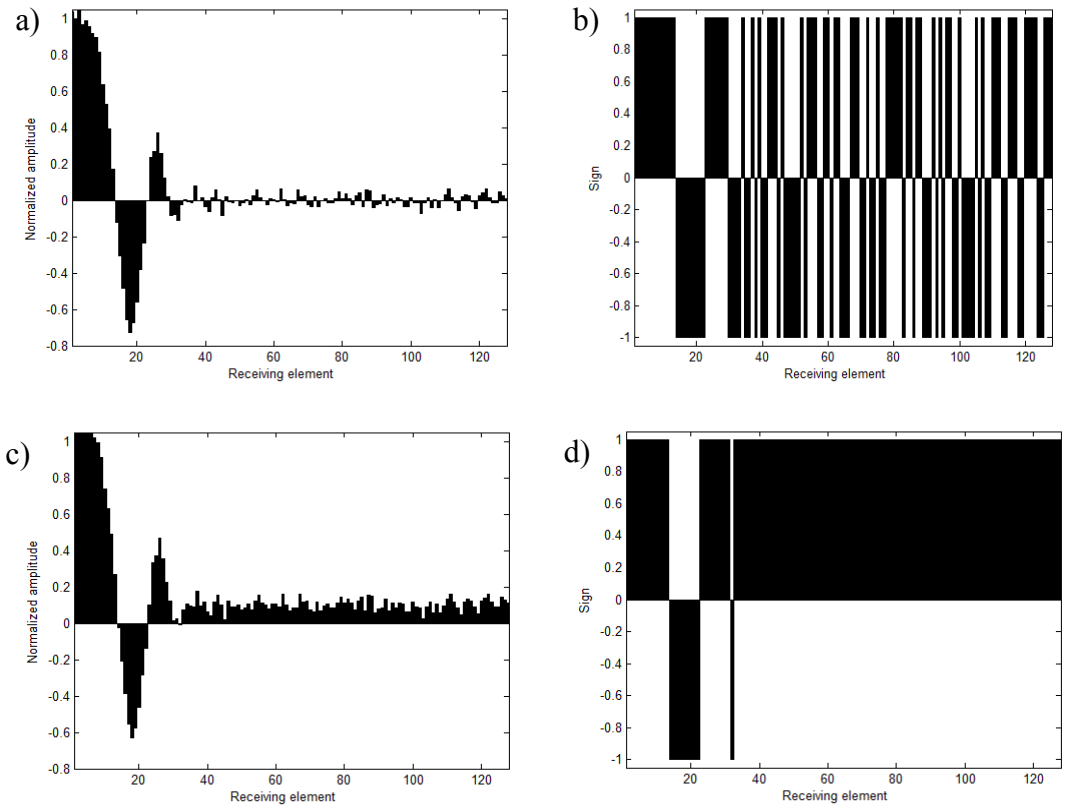

Figure 3 – (a) Amplitude and (b) sign of the signals received across the array elements when emitting with element 1 focusing over an infinite length crack. Same for (c) and (d), but with a finite length crack with the tip at the focus position.

As expected, the signal amplitude reaches unity when emitting and receiving with the first element only, where the specular reflectivity point coincides with the pixel position (R=P). For the remaining elements $t_{ikP} \neq t_{ikR}$, the envelope $E(t_{ikP} - t_{ikR}) < 1$ and the polarity of aperture data change following $\cos(\omega(t_{ikP} - t_{ikR}))$. When the amplitude falls

below the noise level the aperture data signs start showing random values (Figure 3.b). According to (4), the sign coherence factor in this case is $SCF = 0.008$.

Figure 3.c shows the aperture data for a crack that starts at $x = 0$ and extends infinitely to the right. The tip is hence located at the focus position $T = P = (0,-25)$ *mm* and its reflectivity is assumed to be $A_T = -20$ *dB*. While the small offset introduced by A_T in (11) is almost negligible in terms of amplitude (Figure 3.c), it has a significant impact in the aperture data sign distribution (Figure 3.d), grouping them around +1 and rising SCF to 0.49. The ratio between the SCF values in both situations gives an idea of the dynamic range that can be achieved with the SCI image to distinguish the tip from the crack (about 36 dB in this case). This figure mainly depends on the ratio between the crack and the tip reflectivity (A_R / A_T) and on the noise level σ_η.

Figure 4.a shows the ratio between the tip and the crack amplitudes in the Sign Coherence Image (SCI_T / SCI_R) as a function of the tip-to-crack reflectivity ratio A_T/A_R from 0 to -60 dB, with $\sigma_\eta = -40$ *dB* and $A_R = 1$. It is observed that the tip-to-crack ratio in the SCI is rather constant when the tip reflectivity is above the noise level (dotted red line at -40 dB). In this range, the tip indication is about 100 times higher than the crack signal, which indicates that SCI is indeed a good imaging modality for a robust detection of the crack tip.

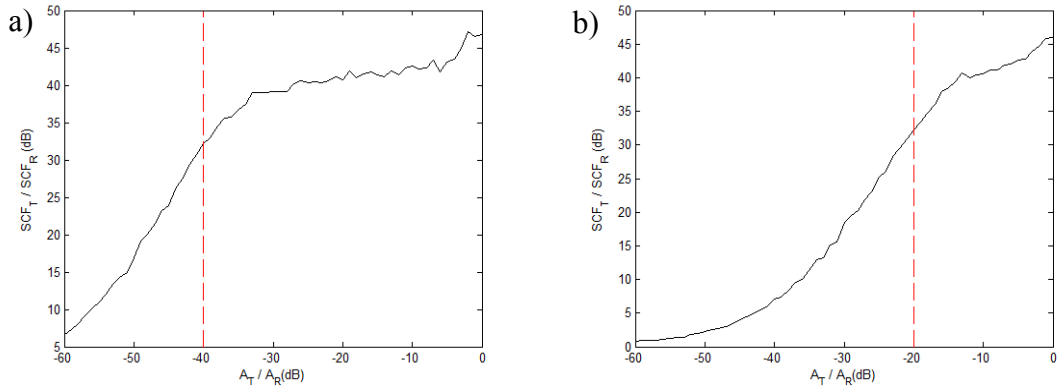

Figure 4 – Tip-crack coherence ratio (SCI_T/ SCI_R) against the tip-crack reflectivity ratio (A_T / A_R) for (a) $\sigma_\eta = -40$ *dB* and (b) $\sigma_\eta = -20$ *dB*.

In practice, the image may be contaminated not only with the amplifiers electric noise (usually low), but also with signal reverberations, converted modes and grain reflections. Figure 4.b shows the tip-crack amplitude ratio when noise increases up to -20 dB, resulting in a tip indication still 20 dB larger than the crack even if its amplitude is -6 dB lower than RMS noise level. This is precisely one of the key features of phase coherence imaging: Improving detection of weak signals (the crack tip) in the presence of high noise or interfering signal levels.

Figure 5 show the TFM and SCI images obtained by numerical simulation for three cracks of 15 mm, 7 mm and 0.5 mm length with 5º, -40º and 30º inclination respectively, using the modified point source simulation model proposed in [35]. The crack was discretized in the image plane with a step of 1/10 lambda, and the signal received by each array element for each TFM emission was calculated by applying the superposition principle of point sources [35]. Finally, the TFM and SCI images were obtained by (2) and (7) respectively. The simulation parameters are the same used

before: $N = 128$, $f = 15\ MHz$, $d = 0.25\ mm$, $bw = 60\%$ and $c = 5.9\ mm/\mu s$, and the cracks were located at $z = -10\ mm$ depth.

The simulation confirms that, for different crack sizes and orientations, the SCI image clearly shows the crack tips, improving the sizing capabilities with regard to the original TFM image. For example, the size of the 15 mm crack inclined 5º is under estimated to 12.5 mm if measured by -6 dB amplitude drop from the TFM image (Figure 5.a), but it is correctly measured from the distance between the tips detected in the SCI image (Figure 5.b). A similar result is obtained for a larger inclination angle of *-40º* in Figures 5.c and 5.d.

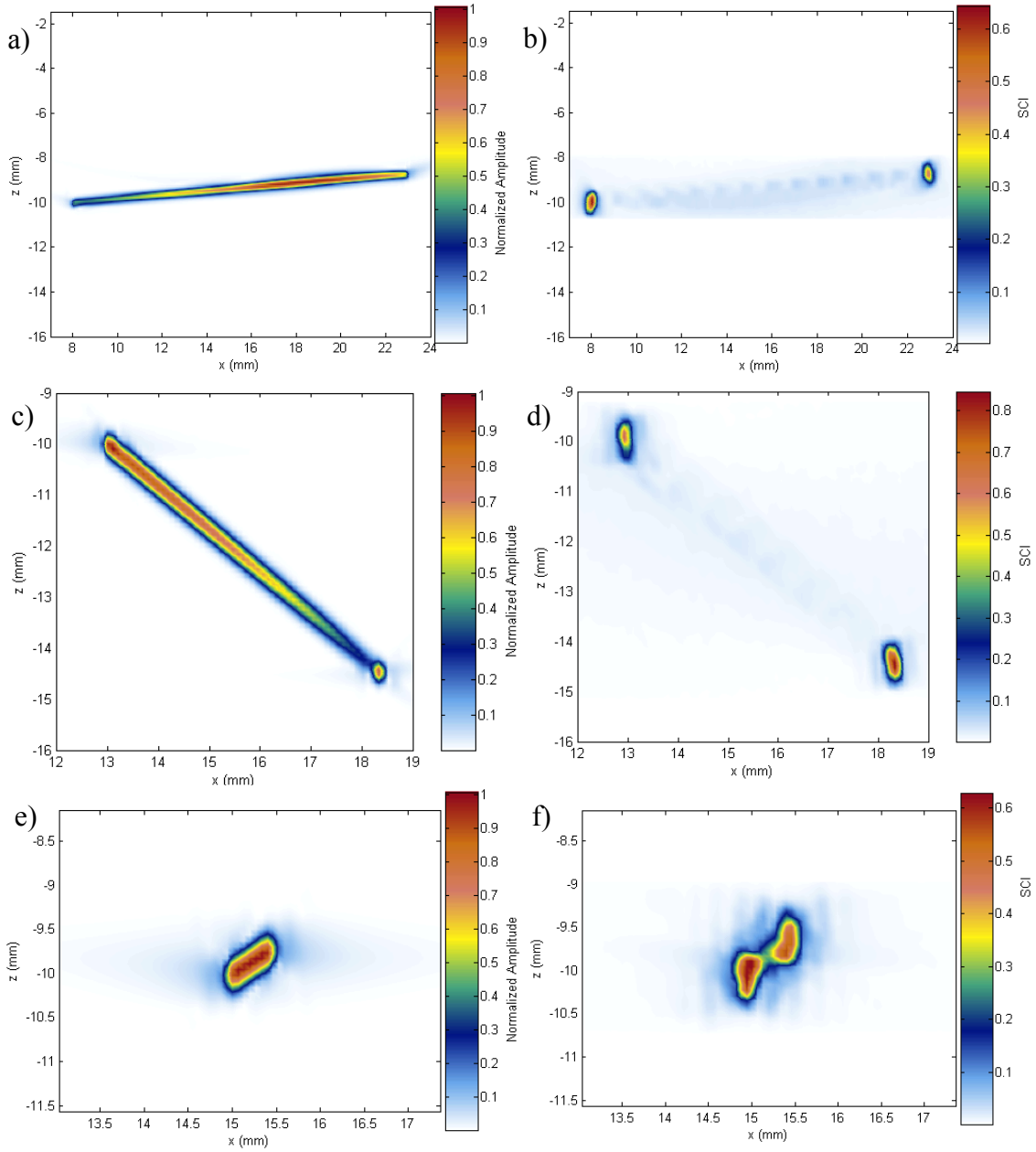

Figure 5 – Numerical simulation of TFM and SCI images (left and right columns respectively) for cracks of different size and orientation (a,b) 15 mm and 5º (c,d) 7 mm and -40º (e,f) 0.5 mm and 30º.

The smaller crack length measurable with the proposed method is given by the main-lobe width of the SCF factor, which is half the width of the main-lobe (between zeros) of the delay-and-sum beamformer [17]. Therefore, the lateral resolution of the SCI image defined by (7) is expected to be similar to the lateral resolution of the TFM image measured at -6 dB. Figure 5.f shows the SCI image of a small crack of 0.5 mm length (≈ 1.2 λ) and 30º inclination, where the tips are clearly detected despite its small size.

3. MATERIALS AND METHODS

Figure 6 shows the experimental set-up used to measure the crack propagation path. Table I summarizes the main parameters of the experimental apparatus used in this work. The array transducer was placed in contact with the lateral side of the sample using coupling gel, and the FMC matrix was captured with a 128 full-parallel ultrasound Phased Array system (model SITAU-111, Dasel, Madrid). A plastic stopper was attached to the left flange of the array to ensure that all the examined samples have the same position relative to the array elements.

A low carbon steel (ASTM A283 grade C) was used to manufacture the CT samples. They were previously subjected to a constant amplitude force controlled fatigue test in a dynamic testing machine (Hung Ta 9711, Korea), according to the parameters shown in Table I. The purpose here was to produce different crack lengths at each sample by varying the number of test cycles. A sample free of crack was also used to obtain the notch tip initial position because once the crack starts propagating, the original notch tip usually disappears from the image. For this reason, the crack length is measured from the left-most detected tip in each image against the position of the original notch tip located in the first image (reference before starting the test). According to the ASTM Standard E-647 [20], the crack length must be referenced to the midpoint between the holding holes centers, which adds a constant offset value to the crack length referenced to the notch tip.

Image formation was performed offline using Python and OpenCL for GPU parallel processing on GPU, while Matlab was used for image representation and analysis. TFM and SCI images were generated over a rectangular grid of 81 x 300 pixels, with a resolution of *0.1 x 0.1 mm* in *x* and *z* respectively.

Figure 6 – Picture of the experimental set-up. Compact Tension sample (according ASTM E647 – 13ae1) along with array transducer of 128 elements operating at 15 MHz.

Parameter	Value
Array Frequency	15 MHz
Array Pitch	0.25 mm
Array Bandwidth	60 %
Array Manufacturer	Imasonic (France)
Material speed of sound	5.901 mm/μs
Sampling frequency	40 MHz
Ultrasound system	SITAU-111, Dasel (Spain)
Sample design	ASTM E647 – 13ae1 test standard (Figure 1)
Fatigue testing parameters	Frequency = 30 Hz, Max load = 4000 N, Load ratio = 0.1 Ambient temperature.
TFM image size	81 x 300 pixels
TFM image resolution	0.1 x 0.1 mm

Table I – Parameters of the experimental set-up

4. EXPERIMENTAL RESULTS

Figure 7.a shows the TFM image of sample nº 1, where a crack is clearly seen. The small black circle marks the position of the original notch tip (obtained from the TFM image of the reference sample), from where the crack grows during the fatigue test (crack root). The TFM image shows a rectilinear trajectory with 2.4º slope, which matches the optical image with manual crack identification (superimposed in Figure 7.a). A direction change is observed near the crack root, which generates a signal amplitude loss in the TFM image. The crack length estimated with the -6 dB amplitude drop criterion is 5.2 mm, while the length optically estimated is 5.25 mm.

Figure 7.b shows the SCI image of the same sample, where a high coherence spot is seen at the tip position. In this case, a second high-coherence indication appears at the location of the original notch tip, probably because of a local peak in the roughness of the crack. This indication usually disappears when the crack continues propagating. For this reason, we propose to measure the crack length by considering the notch tip without crack as a reference (first acquired image), being 5.2 mm for this sample. As expected for a plane reflector, the found tip location reasonably agrees with the -6 dB amplitude drop point of the TFM image, giving equivalent length measurements for this sample. Figure 7.c shows the lateral profile of TFM (black) and SCI (red), which agree with simulation results.

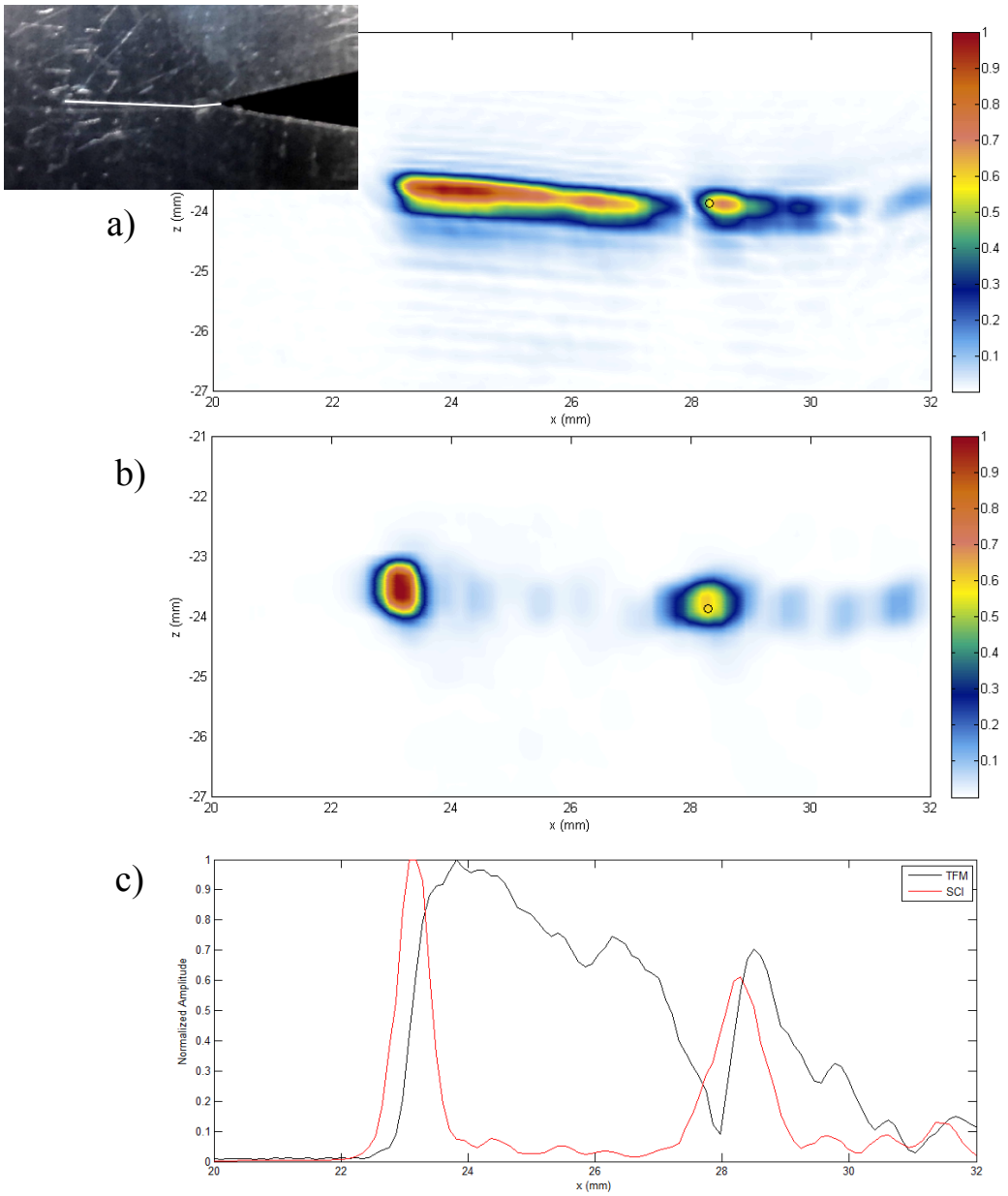

Figure 7 – Images of sample nº 1 (a) TFM with superimposed picture (b) SCI and (c) lateral profiles of TFM (black) and SCI (red).

Figure 8.a shows the optical image of sample nº 2, with the crack path estimated by visual methods. In this case, a more irregular crack was propagated, with several direction changes and surface roughness. Although TFM is less sensitive to crack orientation than, for example, phased-array imaging, local direction changes during propagation introduce variations in the crack amplitude. When the -6dB amplitude drop technique is applied here, measured crack length is 10.3 mm, while reference length obtained by optical method is 13.5 mm. If a -20 dB criterion is used, measured length is 13.6 mm, which is more approximated to the real dimension. It evidences the limitation of sizing methods based on amplitude drop measurements, which greatly depend on the threshold level.

Figure 8.b shows the SCI image of the same sample, where the end tip is clearly detected at $x = 15\ mm$ by the SCI maximum. The estimated crack length is 13.3 mm, similar to the optical measurement.

In this case, the crack roughness generates bright coherence spots along the crack path (see Figure 8.c), caused by intermediate local peaks that act as point-like reflectors. If none of them has higher amplitude than the tip indication, the maximum value of the SCI image can be directly used to identify the tip.

The blue trace in Figure 8.c shows the profile of the coherence-weighted TFM image according to (6). While in the SCI image the brighter spot is given at the crack tip, with the original formulation of SCF the higher value is obtained at x ≈ 20 mm, leading to incorrect sizing. Because the SCI image is not affected by the TFM amplitude, it is more adequate for locating the crack tip than the original SCF formulation (eq. 6).

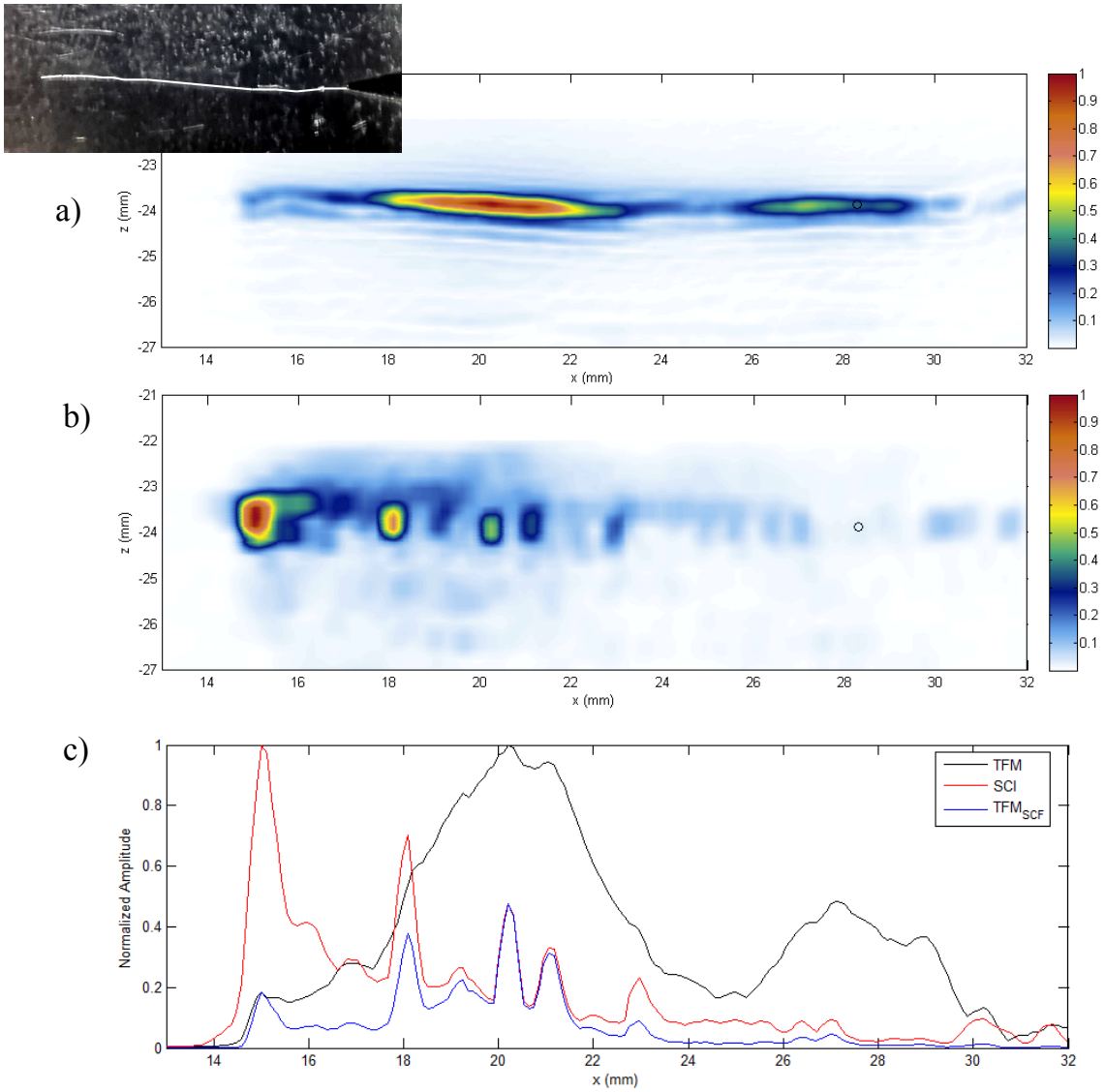

Figure 8 – Images of sample nº 2 (a) TFM with superimposed picture of the crack (b) SCI and (c) lateral profiles of TFM (black), SCI (red) and TFM weighted by SCF according to eq. (6) (blue).

Figures 9 and 10 shows the TFM and SCI images obtained with samples nº 3 and 4, with similar results to those previously analyzed. Again, because of crack surface roughness, multiple tips along the crack path are observed in the SCI image, but maximum coherence always gives at the crack tip. In the TFM images, and despite amplitude variations, the crack path can be followed, and its orientation can be easily estimated.

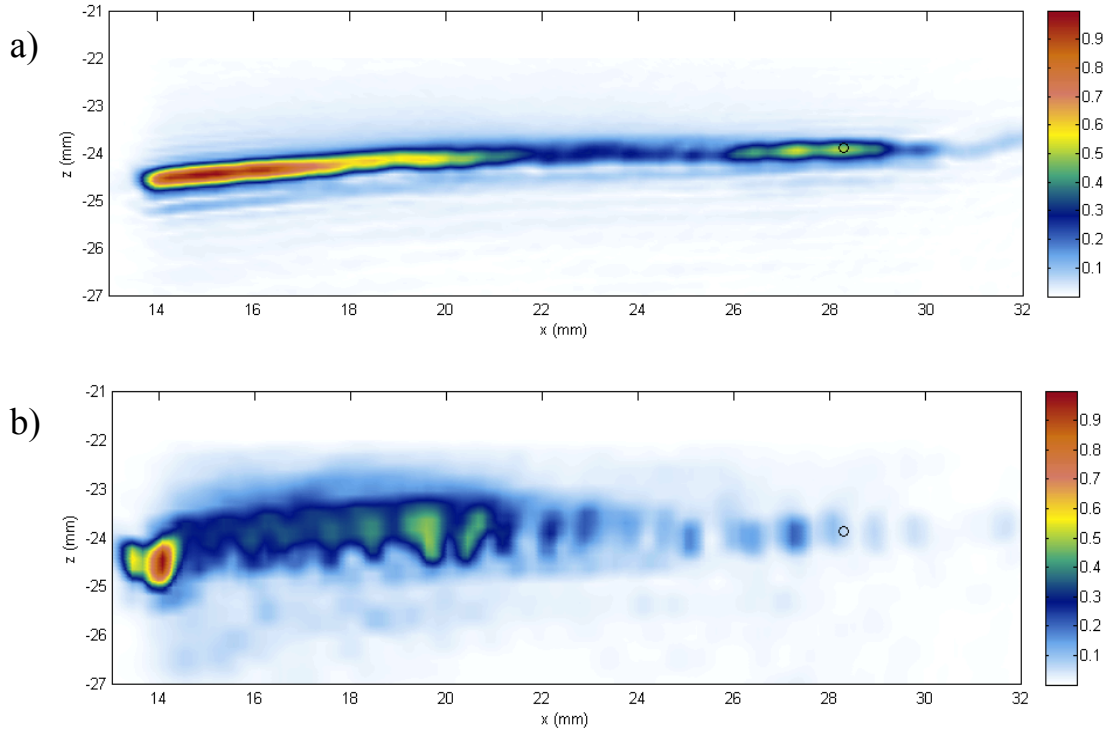

Figure 9 – Images of sample nº 3 (a) TFM (b) SCI.

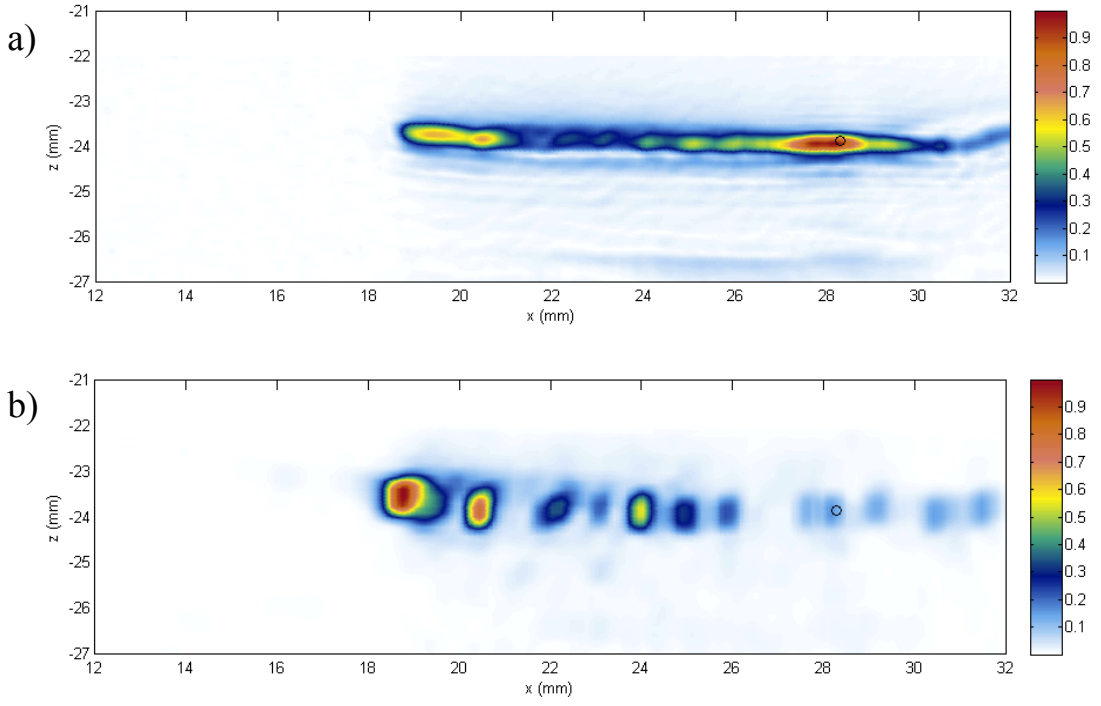

Figure 10 – Images of sample nº 4 (a) TFM (b) SCI.

5. DISCUSSION

Table II summarizes the experimental results. Crack length is correctly estimated either by maximum coherence in the SCI image or by -20 dB signal drop with TFM. However, in TFM, applying a -6 dB amplitude threshold leads to misleading results because the maximum amplitude is not given near the tip. It evidences the problems associated with amplitude drop based methods, mainly for automatic detection algorithms like in this application: A high threshold value, to avoid noise and spurious signals, could detect a local maximum, underestimating the crack length. On the other hand, a low threshold value is more likely to detect the real tip, but the algorithm will be more sensitivity to noise and spurious signals.

Instead, Sign Coherence Image showed the maximum value at the tip location for all the inspected samples, being a more robust method especially for automated algorithms. Crack roughness and direction changes generate bright spots in the SCI image (local maximums), but theoretically, none of them should be larger than the tip indication. Local irregularities should be, in general, more contaminated by close specular reflections, while the crack tip is expected to behave more like a point reflector giving a higher coherence value. In any case, as coherence spots are isolated from each other and they have large contrast with regard to the background, image segmentation and grouping algorithms can be implemented to easily detect all high-coherence points, selecting the farthest one from the root to measure the crack length.

Table II – Summary of experimental results

Sample	Crack Length (mm)				Crack Angle
	Optical	TFM -6dB	TFM -20 dB	SCI Max	
1	5.25	5.2	5.4	5.2	4.4º
2	13.52	10.3	13.6	13.3	1.1º
3	14.27	14.5	14.8	14.2	-2.9º
4	9.42	1.9	9.8	9.5	2.8º

Real-time implementation of the proposed method in a fatigue test machine is feasible with current technology. With an acquisition time of *15 μs,* enough to cover the largest round-trip TOF to the crack, and a sampling frequency of *40 MHz*, the size of the *FMC* matrix is about *20 MB*. With the *USB 2.0* available in the used equipment, up to two datasets per second can be captured. It should be noticed that a fatigue test usually takes minutes or hours, so imaging sampling rate is not needed to be very high. On the host computer side our implementation of TFM and SCI took 0.25 seconds for each image of 80 x 300 pixels, using an AMD Radeon 7770 Core Edition GPU with 2GB RAM, and 640 processors. The limiting factor in this case was data transference time through the USB interface, larger than processing time for each image.

6. CONCLUSION

A new method for ultrasound crack evaluation with arrays was presented, based on the Phase Coherence Imaging principle for extracting the crack tips from the FMC matrix captured with an array. PCI preserves the tip information, which behaves as a point-like reflector, while it attenuates the specular reflections from the crack surface. This way, the crack size can be more easily evaluated by the distance between tips or between the tip and the crack root, from the same FMC matrix captured for TFM. Different from previous approaches, the average of the sign coherence factors (defined as the Sign Coherence Image) is directly used here for crack size evaluation, instead of using them to weight the reflectivity images. By combining TFM and SCI, both the propagation path and the crack length could be determined with high precision and robustness, especially for applications that require automatic evaluation algorithms.

The feasibility of using the proposed method for online monitoring of crack propagation in fatigue tests was corroborated. Crack direction and length obtained showed a good matching with optical measurements, and sizing by tip detection with SCI was more robust than amplitude-drop sizing with TFM. Finally, current processing time of 0.25 s/image allows the use of the proposed method for real-time supervision/recording of progressive changes in fatigue test samples.

ACKNOWLEDGMENTS

This work was partially founded by the projects: ILINK-0988 of the Spanish National Research Council, DPI2013-42236-R of the Spanish Ministry of Economy and Competitivity, PICT-2014-1768 of the ANPCyT and 1106-669-45414 of the “Francisco José De Caldas National Fund for Science, Technology, and Innovation”, Colciencias, Colombia.

REFERENCES

[1] G. Silk, B.H. Lidington, “The potential of scattered or diffracted ultrasound in the determination of crack depth”, Non-Destructive Testing, Volume 8, Issue 3, 1975, Pages 146-151, ISSN 0029-1021.

[2] P. Charlesworth and J. A. G. Temple, “Engineering applications of ultrasonic time-of-flight diffraction”, 2nd Ed., vol. 1. Research Studies Press Somerset, LTD, 2001.

[3] L.W. Schmerr Jr, B. J. Engle, A. Sedov, and X. Li, “Ultrasonic flaw sizing-an overview”, Review of Progress in Quantitative Nondestructive Evaluation, vol. 32, p. 1817, 2013.

[4] K. Manjula, K. Vijayarekha and B. Venkatraman, 2014. Weld Flaw Detection Using Various Ultrasonic Techniques: A Review. Journal of Applied Sciences, 14: 1529-1535.

[5] P. Bastien, “Difficulties in the ultrasonic evaluation of defect size”, Non-Destructive Testing, Volume 1, Issue 3, 1968, Pages 147-151

[6] D. E. MacDonald, “Images of Flaws in Generator Retaining Rings Using SAFT Reconstruction of TOFD Data”, Review of Progress in Quantitative Nondestructive Evaluation, 3, pp 765-772, 1990.

[7] T. Gang & D. Z. Chi, “Novel approach to enhancement of ultrasonic TOFD B-scan image for measurement of weld crack”, Science and Technology of Welding and Joining, 12:1, 87-93, 2007.

[8] F. Jacques, F. Moreau and E. Ginzel, “Ultrasonic back diffraction sizing using phased array – developments in tip diffraction flaw sizing”, Insight, Vol. 45, No. 11, pp. 724-728 November 2003.

[9] J. Mark Davis and Michael Moles, “Resolving Capabilities of Phased Array Sectorial Scans(S-Scans) on Diffracted Tip Signals”, Insight, Vol. 48, no. 4 April 2006, p. 233-239.

[10] Ciorau, P.: "A Contribution to Detection and Sizing Linear Defects by Conventional and Phased Array Ultrasonic Techniques" 16-thWCNDT, Montreal, Aug 30-Sept.03, 2004.

[11] C. Holmes, B. Drinkwater, P. Wilcox, “Post-processing of the full matrix of ultrasonic transmit–receive array data for non-destructive evaluation,” NDT & E International, 38, 8, pp. 701-711, 2005.

[12] J. Zhang, B. W. Drinkwater, P. D. Wilcox, A. J. Hunter, “Defect detection using ultrasonic arrays: The multi-mode total focusing method,” NDT & E International, 43, 2, pp. 123-133, 2010.

[13] Wilcox P D, Holmes C and Drinkwater B “ Enhanced defect detection and characterisation by signal processing of Ultrasonic Array Data” Proc. 9th ECNDT (Berlin) Fr. 1-1-4, 2006.

[14] K. M. M. Tant, A. J. Mulholland and A. Gachagan, "A model-based approach to crack sizing with ultrasonic arrays," in IEEE Transactions on Ultrasonics, Ferroelectrics, and Frequency Control, vol. 62, no. 5, pp. 915-926, May 2015.

[15] J. Zhang, B. W. Drinkwater and P. D. Wilcox, "Defect characterization using an ultrasonic array to measure the scattering coefficient matrix," in IEEE Transactions on Ultrasonics, Ferroelectrics, and Frequency Control, vol. 55, no. 10, pp. 2254-2265, October 2008.

[16] Zhang, J., Drinkwater, B.W. & Wilcox, P.D. “The Use of Ultrasonic Arrays to Characterize Crack-Like Defects” J NondestructEval (2010) 29: 222.

[17] J. Camacho, M. Parrilla, C. Fritsch, “Phase Coherence Imaging”, IEEE Trans. Ultrason. Ferroelectr. Freq. Control, 56, 5, pp. 958-974, 2009.

[18] J. Camacho, C. Fritsch, “Adaptive Beamforming by Phase Coherence Processing”, Ultrasound Imaging, Chap. 4, Ed InTech, 2011.

[19] J. Zhang, B. W. Drinkwater and P. D. Wilcox, "Comparison of ultrasonic array imaging algorithms for nondestructive evaluation," in IEEE Transactions on Ultrasonics, Ferroelectrics, and Frequency Control, vol. 60, no. 8, pp. 1732-1745, August 2013.

[20] ASTM Committee E08.06 on Crack Growth Behavior, ASTM Standard E 647 - 13ae1: Standard Test Method for Measurement of Fatigue Crack Growth Rates, ASTM International, 2013.

[21] J. Barsom y S. Rolfe, Fracture and fatigue control in structures: applications of fracture mechanics, Tercera ed., ASTM, 1999.

[22] D. F. Atehortua López, “Fatigue crack propagation in low carbon and low alloy steel weld joints produced by FCAW and the applicability of ultrasound as a monitoring tool in this kind of studies”. Doctoral dissertation, Facultad de Ingeniería, Universidad del Valle, Cali, Colombia, 2016.

[23] D. Atehortúa, R. Catacolí, Y. Aguilar, H. Sánchez and I. Sabirov, “Development of a physical simulation method of steel welds forfatigue crack propagation studies, on heat affected zones”, Fac. Ing., vol. 25 (42), pp. 33–54 may.-ago. 2016.

[24] Sharpe, W. N., Jr., Jira, J. R., and Larsen, J. M., "Real-Time Measurementof Small-Crack Opening Behavior Using an Interferometric Strain/Displacement Gage," *Small-Crack Test Methods, ASTM STP 1149*, J. M. Larsen and J. E. Allison, Eds., American Societyfor Testing and Materials, Philadelphia, 1992, pp. 92-115.

[25] Resch, M. T. and Nelson, D. V., "An Ultrasonic Method for Measurement ofSize and Opening Behavior of Small Fatigue Cracks," *Small-Crack Test Methods, ASTM STP1149*, J. M. Larsen and J. E. Allison, Eds., American Society for Testing and Materials,Philadelphia, 1992, pp. 169-196.

[26] P. MacLellan, D. Stubbs and P. Karpur, “In-situ ultrasonic surface wave assessment of mechanical fatigue damage accumulation in metal matrix composites”, Composites Engineering, vol. 5, nº 12, pp. 1413-1422, 1995.

[27] S. Rokhlinand J. Kim, “In situ ultrasonic monitoring of surface fatigue crack initiation and growth from surface cavity”, International Journal of Fatigue, vol. 25, nº 1, pp. 41-49, 2003.

[28] T. Roberts and M. Talebzadeh, “Acoustic emission monitoring of fatigue crack propagation”, Journal of Constructional Steel Research, vol. 59, nº 6, p. 695–712, 2003.

[29] Z. Han, H. Luo, J. Cao and H. Wang, “Acoustic emission during fatigue crack propagation in a micro-alloyed steel and welds”, Materials Science and Engineering A, vol. 528, nº 25-26, pp. 7751-7756, 2011.

[30] J. Cao, H. Luo and Z. Han, “Acoustic emission source mechanism analysis and crack length prediction during fatigue crack propagation in 16Mn steel and welds”, Procedia Engineering, vol. 27, pp. 1524-1537, 2012.

[31] Y. Gao, G. Y. Tian, K. Li, J. Ji, P. Wang and H. Wang, “Multiple cracks detection and visualization using magnetic fluxleakage and eddy current pulsed thermography”, Sensors and Actuators A: Physical, vol. 234, pp. 269-281, 2015.

[32] D. Shiozawa, Y. Nakai, T. Murakami and H. Nosho, “Observation of 3D shape and propagation mode transition of fatigue cracks in Ti–6Al–4V under cyclic torsion using CT imaging withultra-bright synchrotron radiation”, International Journal of Fatigue, vol. 58, pp. 158-165, 2014.

[33] Y. Bar-Cohen, S. Kovnovish and E. Harnik, “Direct ultrasonic visualization of fatigue cracks”, NDT International, vol. 13, nº 2, pp. 63-64, 1980.

[34] K. Kimoto, S. Ueno and S. Hirose, “Image-based sizing of surface-breaking cracks by SH-wave array ultrasonic testing”, Ultrasonics, vol. 45, pp. 152-164, 2006.

[35] J. L. Ealo, J. Camacho and C. Fritsch, "Airborne ultrasonic phased arrays using ferroelectrets: a new fabrication approach," in IEEE Transactions on Ultrasonics, Ferroelectrics, and Frequency Control, vol. 56, no. 4, pp. 848-858, April 2009.